

**Autologous chemotaxis at high cell density**Michael Vennettilli,<sup>1,2,\*</sup> Louis González,<sup>1</sup> Nicholas Hilgert,<sup>2,†</sup> and Andrew Mugler<sup>1,2,‡</sup><sup>1</sup>*Department of Physics and Astronomy, University of Pittsburgh, Pittsburgh, Pennsylvania 15260, USA*<sup>2</sup>*Department of Physics and Astronomy, Purdue University, West Lafayette, Indiana 47907, USA*

(Received 6 December 2021; accepted 24 June 2022; published 26 August 2022)

Autologous chemotaxis, in which cells secrete and detect molecules to determine the direction of fluid flow, is thwarted at high cell density because molecules from other cells interfere with a given cell's signal. Using a minimal model of autologous chemotaxis, we determine the cell density at which sensing fails, and we find that it agrees with experimental observations of metastatic cancer cells. To understand this agreement, we derive a physical limit to autologous chemotaxis in terms of the cell density, the Péclet number, and the lengthscales of the cell and its environment. Surprisingly, in an environment that is uniformly oversaturated in the signaling molecule, we find that not only can sensing fail, but it can be reversed, causing backwards cell motion. Our results get to the heart of the competition between chemical and mechanical cellular sensing, and they shed light on a sensory strategy employed by cancer cells in dense tumor environments.

DOI: [10.1103/PhysRevE.106.024413](https://doi.org/10.1103/PhysRevE.106.024413)**I. INTRODUCTION**

One of the more remarkable ways that cells detect the flow direction of a surrounding fluid is through a process called autologous chemotaxis [1,2]. In this process, cells secrete a diffusible ligand that they also detect with surface receptors. The flow biases the ligand distribution such that more ligand is detected by receptors downstream than upstream. This imbalance informs the cell of the flow direction. Autologous chemotaxis has been observed for breast cancer [1,3], melanoma [1], and glioma cell lines [4], as well as endothelial cells [5].

Tumors and endothelia are, by definition, environments with high cell densities. High cell density poses a challenge to the mechanism of autologous chemotaxis: in addition to detecting its own secreted ligand, a cell will detect ligand secreted by nearby cells. In principle, this exogenous ligand could interfere with the information obtained by a cell from its endogenous ligand. Indeed, it has been shown theoretically that the flow-aligned anisotropy of one cell is reduced by a second cell if both are performing autologous chemotaxis [6].

The disruption of autologous chemotaxis at high cell density has been demonstrated experimentally [3]. In fact, at high cell density, cells do not merely stop migrating in the direction of the flow; they migrate against the flow [3]. The reversal is due to a second flow-detection mechanism, distinct from autologous chemotaxis, that relies on focal adhesions and is independent of cell density [3]. Nevertheless, the implication is that for this focal-adhesion-mediated mechanism to dominate at high cell density, autologous chemotaxis must

be weakened at high cell density [3,6]. Indeed, when the focal-adhesion-mediated mechanism is blocked, cells at high density once again migrate with the flow but at a directional accuracy reduced from that of cells at low density without the block [3].

Here we investigate the failure of autologous chemotaxis at high cell density. First, we numerically solve the fluid-flow and advection-diffusion equations for a given cell density in a confined environment, and we find that a cell's anisotropy falls off at a density consistent with experimental observations [3]. To explain this agreement, we derive a physical limit to autologous chemotaxis at high cell density, which successfully predicts the falloff density as a function of the Péclet number and the cell and confinement lengthscales. Finally, we predict that in the presence of an oversaturated amount of background ligand, which can occur, e.g., if some cells secrete but do not absorb ligand, the anisotropy detected by an absorbing cell can actually reverse directions. This reversal is distinct from that due to the focal-adhesion-mediated mechanism [3] but is relevant to scenarios in which nonchemotaxing cells provide additional ligand secretion, as in the case of lymphatic endothelial cells [1].

**II. RESULTS**

We consider a minimal model of autologous chemotaxis, in which each cell is a sphere of radius  $a$  within a background flow of speed  $v_0$  (Fig. 1). We focus on a cell's initial ability to detect a bias in the ligand field, before cell movement causes significant rearrangement of cell positions, and therefore we treat each cell as stationary. A cell secretes ligand at a rate  $\nu$  and absorbs ligand at a rate  $\mu$ . We consider two cases for ligand detection: the cell either reversibly binds ligand molecules, corresponding to  $\mu = 0$ ; or the cell absorbs ligand molecules (e.g., via receptor endocytosis), corresponding to a finite value of  $\mu$ . For absorption, we take  $\mu/aD = \pi(\sqrt{17} -$

\*Present address: AMOLF, 1098 XG Amsterdam, The Netherlands.

†Present address: Department of Systems Biology, Harvard Medical School, Boston, MA 02115, USA.

‡andrew.mugler@pitt.edu

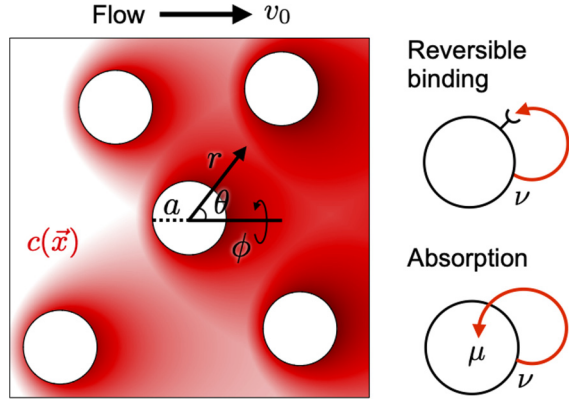


FIG. 1. Autologous chemotaxis with multiple cells. Each cell of radius  $a$  secretes and detects ligand (red). Secretion occurs at rate  $\nu$ . Detection occurs by reversible binding ( $\mu = 0$ ) or absorption ( $\mu > 0$ ). Fluid flow at background speed  $v_0$  biases the ligand concentration  $c(\vec{x})$ . The anisotropy of the detected signal at the surface of the cell of interest distinguishes its downstream ( $\theta = 0$ ) and upstream ( $\theta = \pi$ ) sides.

1)  $\approx 10$ , where  $D$  is the ligand diffusion coefficient, which maximizes sensory precision in this case [2]. Given that the timescales of binding [2], dimerization [7], and endocytosis [8] of the CCR7 receptor responsible for autologous chemotaxis are on the order of minutes, which is faster than the time required to reliably establish anisotropy (several hours [2]), we ignore these processes and characterize detection with the single absorption rate  $\mu$ .

In either the reversible binding or absorption case, we calculate the normalized anisotropy measure [2,9,10]

$$A = \frac{\int d\Omega c(a, \theta, \phi) \cos \theta}{\int d\Omega' c(a, \theta', \phi')} \quad (1)$$

for a given cell from the steady-state ligand concentration  $c(r, \theta, \phi)$  at the cell surface  $r = a$ , where  $d\Omega = d\phi d\theta \sin \theta$ . The cosine extracts the asymmetry of the concentration between the downstream ( $\theta = 0$ ) and upstream ( $\theta = \pi$ ) sides the cell, such that downstream bias corresponds to  $A > 0$  whereas upstream bias corresponds to  $A < 0$ .

### A. Numerical solution

Although the anisotropy can be obtained analytically to a good approximation for a single cell [2] or two cells [6], the presence of multiple cells breaks the symmetry of the flow lines and ligand concentration field, making an analytic solution intractable. Therefore, we first turn to a numerical solution. Specifically, for a given cell configuration, we use the finite-element software COMSOL to solve in steady state (i) the Brinkman equation [11] for the flow velocity field, which is appropriate for low-Reynolds-number, low-permeability flow as in the experiments [1,3]; and (ii) the advection-diffusion equation for the ligand concentration, where the solution to the Brinkman equation provides the advection term. A cell of interest is placed at the center of a box with length  $L$ , width  $W$ , and height  $H$  (where  $L$  is in the flow direction), and other cells are placed randomly such that no cell overlaps a box wall

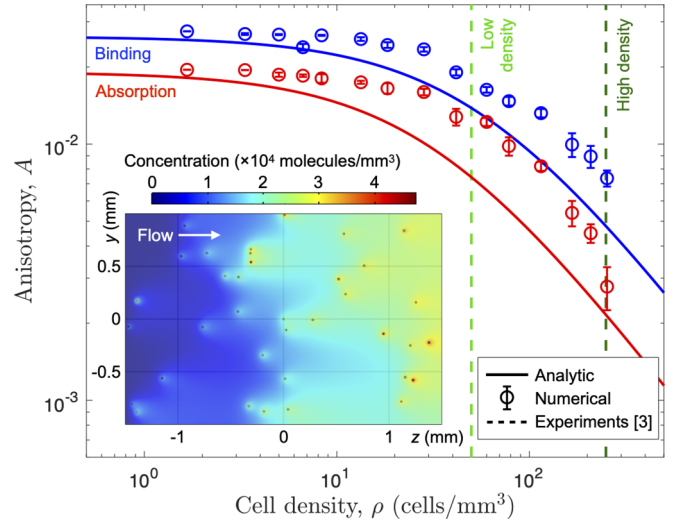


FIG. 2. Failure of autologous chemotaxis at high cell density. Data points: Anisotropy  $A$  at the center cell, averaged from the numerical solution of five configurations per cell density  $\rho$  (error bars, standard error). Curves: Analytic approximation [Eq. (8)]. Dashed lines: Experimental seeding densities at which cells were observed to migrate with the flow (low density) and against the flow (high density) [3]. See text for parameter values. Inset: Numerical steady-state concentration profile for an example configuration of 36 cells ( $\rho = 60$  cells/mm<sup>3</sup>) with absorption.

or another cell. See Appendix A for details of the numerical solution. Our COMSOL code is freely available [12].

We obtain the model parameters from the experiments. A breast cancer (MDA-MB-231) cell is approximately  $a = 10 \mu\text{m}$  in radius [1,3] and secretes approximately  $\nu = 1$  ligand molecule per second [1,2], which diffuses with approximate coefficient  $D = 150 \mu\text{m}^2/\text{s}$  [13]. The cell density experiments [3] were performed with flow velocity  $v_0 = 3 \mu\text{m}/\text{s}$  and permeability  $\kappa = 0.1 \mu\text{m}^2$  in a chamber with length approximately  $L = 3$  mm, width approximately  $W = 2$  mm, and height, to the best of our knowledge, on the order of  $H = 100 \mu\text{m}$  (we will see that our theoretical results do not depend on  $H$ ).

An example of the resulting concentration profile is shown in Fig. 2 (inset). The left-right asymmetry in the concentration profile is due to the rightward flow. The flow biases a given cell's steady-state concentration profile to the right. With many cells in the box, and given the long-range ( $1/r$ ) nature of the profiles, these biases result in a buildup of concentration on the right side of the box.

The anisotropy at a given cell density  $\rho$  is obtained via Eq. (1) from the concentration profile at the center cell's surface, averaged over multiple configurations of the other cells. The anisotropy as a function of cell density is shown in Fig. 2 (data points). Also shown are the experimental densities (dashed lines) at which cells were observed to migrate with the flow (low density) and against the flow (high density) [3].

We see in Fig. 2 that the experimental densities occur in the regime where the anisotropy transitions from its maximal value to a falloff toward zero. If, instead, the experimental densities were much smaller, then both predicted anisotropy values would be near-maximal, and at both densities cells

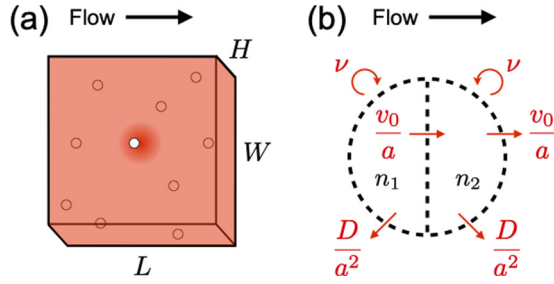


FIG. 3. Derivation of the physical limit. (a) The mean-field model approximates ligand concentration from all cells other than the cell of interest as uniform. (b) Anisotropy approximated as the difference in ligand number between halves of a permeable cell. Secretion, flow, and diffusion set entry and exit rates.

would be expected to migrate downstream. Conversely, if the experimental densities were much larger, then both predicted anisotropy values would be very small, and at both densities cells would be expected to migrate upstream due to the competing focal-adhesion-mediated mechanism. Thus, our numerical solution is quantitatively consistent with the hypothesis that only cells at high density experience a sufficient failure of autologous chemotaxis that the focal-adhesion-mediated mechanism would be able to take over [3].

### B. Mean-field approximation

The numerical solution gives a quantitative prediction for the falloff of anisotropy with cell density, but it does not provide physical intuition. On what parameters does the falloff depend, and why does the transition density occur where it does? To address these questions, we introduce and solve a mean-field model. The result will be a physical limit to autologous chemotaxis that agrees well with the numerical results and predicts the transition density analytically.

The mean-field model approximates the ligand from all cells other than the cell of interest as a uniform background concentration  $c_0$  [Fig. 3(a)]. This approximation is clearly incongruous with the observation of a nonuniform concentration field in the simulations (Fig. 2, inset). Our aim is to investigate the extent to which the mean-field results hold despite this incongruity. The problem now consists of two parts: (i) determine the anisotropy  $A$  as a function of  $c_0$ , and (ii) determine  $c_0$  as a function of the cell density  $\rho$ .

#### 1. Anisotropy versus background concentration

To determine the anisotropy as a function of background concentration, we will generalize our perturbative solution for a single cell [2] to include a uniform background concentration  $c_0$ . First, however, we provide a simple argument for how this expression should scale. The result of the scaling argument will turn out to be different from the rigorous solution only by two numerical factors.

Imagine for a moment that the cell is permeable to both the ligand [14] and fluid [Fig. 3(b)]. Permeability to the fluid will neglect the effects of laminar flow around the cell but will permit a simple counting exercise. Specifically, we hypothesize that the anisotropy is roughly equivalent to the difference in the number of molecules in the downstream and

upstream halves of the cell, normalized by the total number [15]. These molecule numbers can be obtained approximately by considering the rates of molecule arrival to and departure from each half [Fig. 3(b)]. Molecules arrive in the vicinity of each half due to secretion, at a rate  $v$ . Molecules depart from each half due to diffusion away from the cell, from which a rate can be constructed using the cell radius as  $D/a^2$ . Finally, molecules depart the upstream half due to flow, at a similarly constructed rate  $v_0/a$ . Molecules also depart the downstream half, but this departure is compensated by the arrival of the upstream half's molecules, resulting in no net loss due to flow. The molecule number in each half is then the ratio of arrival rates to departure rates, giving a difference of

$$\Delta n \sim \frac{v}{D/a^2} - \frac{v}{D/a^2 + v_0/a} \approx \frac{\epsilon v a^2}{D}, \quad (2)$$

where the second step introduces the Péclet number  $\epsilon \equiv v_0 a/D$  and recognizes it as a small parameter (indeed, the experimental values above give  $\epsilon = 0.2$ ). The molecule number in the whole cell is twice that of either half, or, ignoring the factor of 2,  $n \sim v a^2/D$ .

Now consider the addition of a uniform background concentration of ligand  $c_0$ . The background does not change the difference  $\Delta n$ , but it does change the total molecule number  $n$ . Specifically,  $n$  increases by the number of background ligand molecules in the cell volume, which scales as  $c_0 a^3$ , giving  $n \sim v a^2/D + c_0 a^3$ . Combining this expression with Eq. (2), we obtain

$$A \sim \frac{\Delta n}{n} \sim \frac{\epsilon v}{v + c_0 a D} \quad (3)$$

as a scaling estimate for the anisotropy.

We compare this estimate with a rigorous calculation of the anisotropy in the presence of a uniform background concentration that we perform by generalizing our previous work using the Péclet number as a perturbation parameter [2]. The result, derived in Appendix B, is

$$A = \frac{f \epsilon (v - \mu c_0)/8}{v + 4\pi c_0 a D}, \quad (4)$$

where  $f \equiv (1 + \mu/8\pi a D)^{-1}$ . In the limit of reversible binding ( $\mu \rightarrow 0$ ), this result simplifies to

$$A = \frac{\epsilon v/8}{v + 4\pi c_0 a D}. \quad (5)$$

Comparing Eqs. (3) and (5), we see that the scaling estimate is accurate apart from two numerical factors (1/8 in the numerator and  $4\pi$  in the denominator).

#### 2. Background concentration versus cell density

To determine the background concentration  $c_0$  as a function of the cell density  $\rho$ , we present a simple flux argument. Molecules enter the box due to secretion by cells and leave the box due to (i) absorption by cells and (ii) flow. Specifically, the flux of molecules entering the box per unit time is equal to the secretion rate per cell  $v$  times the number of cells in the box  $\rho LWH$ . The flux of molecules leaving the box

per unit time contains two terms. The first is equal to the absorption rate at each cell's surface  $\mu c_0$  times the number of cells in the box  $\rho LWH$ , where we have approximated the surface concentration as the background concentration  $c_0$ . The second is equal to the background concentration  $c_0$  times the volume of fluid leaving the box per unit time, which is the flow velocity  $v_0$  times the area of the outlet wall  $WH$  [Fig. 3(a)]. At steady state, these fluxes balance,

$$\underbrace{v\rho LWH}_{\text{flux in}} = \underbrace{\mu c_0 \rho LWH + c_0 v_0 WH}_{\text{flux out}}. \quad (6)$$

Solving Eq. (6) for  $c_0$ , we obtain

$$c_0 = \frac{vL\rho}{\mu L\rho + v_0}, \quad (7)$$

which relates the background concentration  $c_0$  to the cell density  $\rho$ .

### 3. Physical limit

Inserting Eq. (7) into Eq. (4), we obtain

$$A = \frac{f\epsilon/8}{1 + \rho/\rho_c}, \quad (8)$$

where  $\rho_c \equiv g\epsilon/4\pi a^2 L$  with  $g \equiv (1 + \mu/4\pi aD)^{-1}$ . Equation (8) demonstrates that the anisotropy falls off with cell density, as expected, and gives the physical parameters on which the falloff depends. In particular,  $\rho_c$  is the transition density, where the anisotropy is half of its maximal value. The transition density can never be larger than its value in the reversible binding limit ( $\mu \rightarrow 0$ ), i.e.,

$$\rho_c \leq \frac{\epsilon}{4\pi a^2 L}. \quad (9)$$

Equation (9) reveals that the transition density scales with the Péclet number  $\epsilon$  and inversely with a characteristic volume consisting of the cell surface area  $4\pi a^2$  and the system length-scale in the flow direction  $L$ .

Equation (9) represents a physical limit: the maximum cell density for which autologous chemotaxis can succeed, dependent only on the physical properties of the system  $\epsilon$ ,  $a$ , and  $L$ . It also has an intuitive interpretation: scaling lengths by  $a$  such that  $\rho_c a^3 \leq (\epsilon/4\pi)/(L/a)$ , we see that the maximum density increases as (i) the Péclet number  $\epsilon$  increases or (ii) the flow-aligned confinement length  $L$  decreases. The former makes sense because flow is easier to detect with diffusible molecules for a large Péclet number. The latter makes sense because a smaller flow-aligned length places more cells transverse to the flow, where their secreted ligand interferes less with the autologous chemotaxis mechanism of a given cell [6].

We see in Fig. 2 that Eq. (8) (curves) agrees with the numerical results (data points). In particular, the theory predicts the  $\rho^{-1}$  falloff observed numerically and predicts the observed transition densities in both the reversible binding (blue) and absorbing (red) cases up to a factor of approximately 2. The agreement is particularly remarkable because the theory ignores the laminar flow lines from all cells but the cell of interest, and it assumes that the ligand from these cells is uniformly distributed, which, as seen in the inset of Fig. 2, is clearly not the case. We therefore conclude that

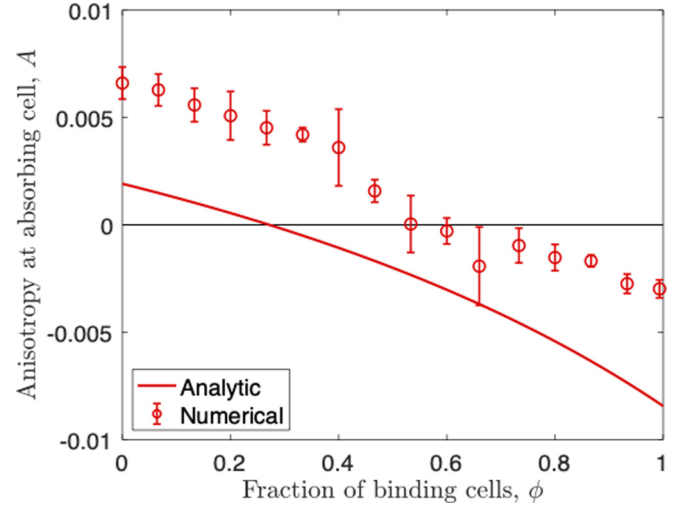


FIG. 4. Chemotactic reversal of anisotropy. A fraction  $\phi$  of cells are binding with the rest absorbing. Anisotropy is measured at the absorbing center cell. Data points: Anisotropy averaged from the numerical solution of five configurations per  $\phi$  value (error bars, standard error). Curve: Analytic approximation [Eq. (10)].  $\epsilon = 0.2$ ,  $\mu/aD = 0$  (binding) or 10 (absorbing), and  $\phi_c = 0.27$  corresponding to 150 cells ( $\rho = 250$  cells/mm<sup>3</sup>).

these details are not essential to the basic physics, and the mean-field theory suffices to quantitatively capture the key dependencies.

### C. Chemotactic reversal

Returning now to Eq. (4), we see that  $A$  becomes negative if  $c_0 > c_0^*$ , where  $c_0^* \equiv v/\mu$ . This result means that for a sufficiently large background concentration, the bias in the ligand signal detected by the cell reverses direction. This result only occurs for absorption, not reversible binding, because in the binding case ( $\mu \rightarrow 0$ ) we see that  $c_0^* \rightarrow \infty$ . It also cannot occur if the background concentration is supplied by other similar cells at density  $\rho$ , as has been assumed so far, at least under the approximation that the background concentration is uniform. Specifically, writing Eq. (7) as  $c_0 = c_0^*/(1 + v_0/\mu L\rho)$  shows that  $c_0 < c_0^*$  in this case, no matter how large  $\rho$  becomes. However, the result can occur if the background concentration is supplied independently of the secrete-and-detect mechanism employed by the cell of interest, for example by other cells of a different type, or if cells are not all identical, as has been assumed so far.

To test this prediction, we once again perform numerical computations as above, but this time instead of using identical cells we use a mix of absorbing and binding (nonabsorbing) cells. Specifically, we keep the center cell absorbing and vary the fraction  $\phi$  of all cells that are binding. Figure 4 (data points) shows the resulting anisotropy  $A$  at the center cell for the high experimental cell density ( $\rho = 250$  cells/mm<sup>3</sup>). We see that as  $\phi$  increases, such that the absorbing cell at the center is in the presence of increasingly more nonabsorbing cells,  $A$  becomes negative, corresponding to a reversal of its bias direction.

The change in sign of  $A$  with  $\phi$  also emerges from the mean-field theory. Reducing net absorption in the background

cells but not the center cell corresponds to taking  $\mu \rightarrow (1 - \phi)\mu$  in Eq. (7) but not Eq. (4). The result is

$$A = \frac{f\epsilon}{8} \left[ \frac{\phi_c - \phi}{\phi_c + (1 - \phi) + 4\pi aD/\mu} \right], \quad (10)$$

where  $\phi_c \equiv \epsilon D/\mu\rho aL$ . Equation (10) is plotted in Fig. 4 (curve), and we see qualitative agreement with the numerics, with a similar quantitative discrepancy to that in Fig. 2 due to the known limitations of the mean-field approximation.

Why does the anisotropy reverse sign for large background concentration? The reason is that, because of the flow, the background ligand is absorbed preferentially at the upstream side of the cell (like mist preferentially wetting one side of an object in a steady wind). For a sufficiently large background concentration and absorption rate, this upstream bias can overpower the downstream bias of the autologous chemotaxis mechanism. This is why there is no reversal for a cell that employs reversible binding: reversible binding gives molecules that bind upstream a chance to also bind downstream. This is also why there is no reversal when all cells are absorbing: sufficient absorption at the cell of interest would imply large absorption by the other cells, which would then necessarily lower the background concentration. Ultimately, chemotactic reversal requires that the exogenous ligand be in excess, i.e., supplied by cells that secrete more or absorb less than the detecting cell.

### III. DISCUSSION

We have investigated the physical mechanisms behind a remarkable form of flow detection, and how the chemical sensing on which this process depends breaks down at high cell densities. By numerically solving the fluid-flow and advection-diffusion equations, we predicted the regime of cell densities at which sensing fails, and we found that our predictions agree with experimental observations. By solving a mean-field model and using simple scaling arguments, we revealed how this critical density depends on the system parameters, thereby providing a physical limit for the maximum cell density at which this type of sensing can succeed. Surprisingly, we observed that in an environment supersaturated in the sensed chemical (i.e., more than that secreted by the cells themselves), the signal can reverse directions due to an abundance of exogenous chemical absorbed at the upstream side of the cell, predicting a chemically mediated reversal distinct from the mechanically mediated reversal observed in experiments. The results herein deepen our physical understanding of a process that guides cancer cell invasion [1,3,4], particularly in dense environments.

The chemically mediated reversal we observe here (Fig. 4) is not relevant to the existing experiments [3] per se: all cells there were of the same type, and therefore these experiments correspond more closely to our scenario of like cells (Fig. 2) than cell mixtures (Fig. 4). Indeed, in the experiments at high cell density, blocking the focal-adhesion-mediated mechanism resulted in largely unbiased (rather than upstream) migration, and blocking autologous chemotaxis resulted in stronger upstream migration [3]; both findings suggest that autologous chemotaxis is weakened, not reversed, at high cell density with like cells. Nevertheless, we predict that

chemically mediated reversal can occur in the presence of excess exogenous ligand from unlike cells, which is a highly plausible scenario *in vivo*. The particular ligand types involved in autologous chemotaxis (chemokines CCL19 and CCL21) are omnipresent in the tumor microenvironment [16–19] and are explicitly secreted by lymphatic endothelial cells that co-exist with the cancer cells in which autologous chemotaxis was first observed [1].

At low cell densities, autologous chemotaxis outcompetes pressure sensing at both high and low flow speeds [3]. Our previous work suggests that cells perform autologous chemotaxis with a precision that approaches the physical limit [2]. This finding helps explain why changing the physical environment by increasing cell density is sufficient to cause autologous chemotaxis to fail. On the other hand, the physical limit to the precision of pressure sensing [20], with which autologous chemotaxis competes, is poorly understood for these cells [3]. Therefore, it is an open question whether pressure sensing is subdominant to autologous chemotaxis at low cell density for biological reasons or by physical necessity.

Autologous chemotaxis fails at high cell densities because the concentration profile in the vicinity of a given cell is homogenized due to ligand secreted by other cells. In principle, this homogeneity could be avoided by known mechanisms that preserve spatial or temporal heterogeneity. For example, cells generally are not distributed uniform-randomly as assumed here. In the experiments [3], cells were observed to migrate in chains that followed the flow lines. During metastatic invasion, cells are known to migrate in chains, sheets, clusters, or aggregates [21–26]. Alternatively, secreting and detecting the ligand in temporal pulses could help a given cell distinguish its endogenous ligand from exogenous ligand secreted by other cells at other times. Although the dynamics of chemokine release are still poorly understood, single temporal pulses of chemokine release are sufficient to generate responses at the cell level [27].

Finally, a ubiquitous way that cells at high densities detect weak signals, including concentrations [28–30] and concentration gradients [31–33], is by acting collectively [10,15,34,35]. While here we have elucidated how high cell density is detrimental to autologous chemotaxis performed by a single cell, high cell density may be beneficial if an analogous computation is performed at the collective level. Whether autologous chemotaxis benefits from collective effects remains an open question.

### ACKNOWLEDGMENTS

We thank Hye-ran Moon and Bumsoo Han for help with COMSOL in the early stages of the work. This work was supported by Simons Foundation Grant No. 376198 and National Science Foundation Grants No. MCB-1936761 and No. PHY-1945018.

### APPENDIX A: DETAILS OF NUMERICAL SOLUTION

We obtain the numerical solution using the finite-element software COMSOL. The boundary conditions are set as follows [3]. For the Brinkman equation, cell surfaces and side walls are no-slip boundaries, whereas the upstream wall is an

inlet boundary with flow speed  $v_0$ , and the downstream wall is an outlet boundary with zero pressure. For the advection diffusion equation, the side walls are no-flux boundaries, the upstream wall is an inflow boundary (zero concentration), the downstream wall is an outflow boundary (no flux), and cell surfaces are flux boundaries with secretion and absorption rates  $\nu$  and  $\mu$ , respectively.

Specifically, the flux boundary condition in COMSOL reads

$$-\vec{n} \cdot (\vec{J} + \vec{v}c) = k_c(c_b - c). \quad (\text{A1})$$

Because the normal vector  $\vec{n}$  is parallel to the outward flux  $\vec{J} = D\partial_r c \hat{r}$  at the spherical boundary  $r = a$ , and the flow velocity  $\vec{v}$  vanishes at the cell surface, Eq. (A1) simplifies to

$$-D\partial_r c|_a = k_c c_b - k_c c|_a. \quad (\text{A2})$$

Comparing this condition with our secretion/absorption condition [2]

$$-4\pi a^2 D\partial_r c|_a = \nu - \mu c|_a, \quad (\text{A3})$$

we see that

$$k_c = \frac{\mu}{4\pi a^2}, \quad c_b = \frac{\nu}{\mu}. \quad (\text{A4})$$

We use these expressions, with  $a = 10 \mu\text{m}$ ,  $D = 150 \mu\text{m}^2/\text{s}$ ,  $\nu = 1/\text{s}$ , and a given  $\mu$ , to set  $k_c$  and  $c_b$ . For the absorbing case, we use  $\mu/aD = \pi(\sqrt{17} - 1)$  to set  $\mu$ . For the binding case, because we cannot take  $\mu$  strictly to zero, we use  $\mu/aD = 10^{-3} \ll 1$  to set  $\mu$ .

The permeability estimated in the experiments is  $\kappa = 0.1 \mu\text{m}^2$  [3], which is much lower than the cross-sectional area of a cell, i.e.,  $\kappa/a^2 = 10^{-3} \ll 1$ . We find that using such a low permeability in COMSOL introduces numerical instability. Therefore, we use a value 10 times higher,  $\kappa = 1 \mu\text{m}^2$ , for which  $\kappa/a^2 = 10^{-2}$ , which still satisfies  $\kappa/a^2 \ll 1$ . We find essentially no difference between  $\kappa/a^2 = 10^{-3}$  and  $10^{-2}$  in the single-cell analytic solution [2] because the system is so deeply within the low-permeability regime.

To correct for any numerical error introduced by COMSOL, we calibrate the numerical anisotropy values to the analytic solution  $A_a = \epsilon/(8 + \mu/\pi aD)$  for a single cell [Eq. (4)], which we know is accurate to within 0.4% [2]. Specifically, for each of the two  $\mu$  values, we calculate the anisotropy  $A_n$  from the numerical solution for a single cell in a sufficiently large box to be approximated as infinite. We find that the existing box dimensions  $L = 3 \text{ mm}$  and  $W = 2 \text{ mm}$  are sufficiently large that  $A_n$  no longer changes as either is increased, whereas the box dimension  $H = 100 \mu\text{m}$  must be increased to 1 mm to satisfy this condition. We then multiply the numerical anisotropy values (with  $H$  back to  $100 \mu\text{m}$ ) by  $A_a/A_n$  to enforce the calibration.

COMSOL and MATLAB code is freely available [12].

## APPENDIX B: ANALYTIC SOLUTION WITH BACKGROUND CONCENTRATION

We solve for the anisotropy for a single cell with a uniform ligand background concentration following our previous solution for no background concentration [2]. We begin by

defining the nondimensionalized variables

$$\chi \equiv ca^3, \quad x \equiv \frac{r}{a} \quad (\text{B1})$$

and parameters

$$\beta \equiv \frac{\nu a^2}{4\pi D}, \quad \alpha \equiv \frac{\mu}{4\pi aD}, \quad \zeta \equiv \frac{\sqrt{\kappa}}{a}. \quad (\text{B2})$$

In these terms, the steady-state diffusion-with-drift equation for the ligand concentration reads

$$0 = \nabla_x^2 \chi - \epsilon \vec{u} \cdot \vec{\nabla}_x \chi, \quad (\text{B3})$$

where  $\epsilon \equiv v_0 a/D$  is the Péclet number, and

$$\vec{u}(x, \theta) = \frac{\vec{v}(x, \theta)}{v_0} = u_x(x) \cos \theta \hat{x} - u_\theta(x) \sin \theta \hat{\theta} \quad (\text{B4})$$

is the nondimensionalized flow field, with

$$u_x(x) \equiv 1 - \frac{Z}{x^3} + \frac{3\zeta}{x^2} \left(1 + \frac{\zeta}{x}\right) e^{(1-x)/\zeta},$$

$$u_\theta(x) \equiv 1 + \frac{2Z}{x^3} - \frac{3}{2x} \left(1 + \frac{\zeta}{x} + \frac{\zeta^2}{x^2}\right) e^{(1-x)/\zeta}, \quad (\text{B5})$$

and  $Z \equiv 1 + 3\zeta + 3\zeta^2$  [36].

We solve Eq. (B3) through the method of matched asymptotic expansions [37], using  $\epsilon \ll 1$  as our expansion parameter. The inner expansion, valid near the cell surface, is

$$\chi(x, \theta) = \chi_0(x, \theta) + \epsilon \chi_1(x, \theta) + O(\epsilon^2). \quad (\text{B6})$$

We will see that  $\chi_0$  is isotropic, and therefore to find the anisotropy, we will need to solve the inner expansion out to  $\chi_1$ . The inner expansion satisfies the boundary condition at the cell surface, which reads

$$-\partial_x \chi|_{x=1} = \beta - \alpha \chi(1, \theta) \quad (\text{B7})$$

from Eq. (A3).

The outer expansion is valid far from the cell surface. Therefore, we define a rescaled distance  $s \equiv \epsilon x$  and denote the outer expansion as  $X(s, \theta)$ . In terms of  $s$ , Eq. (B3) reads

$$0 = \nabla_s^2 X - \vec{u}(s/\epsilon, \theta) \cdot \vec{\nabla}_s X. \quad (\text{B8})$$

From Eqs. (B4) and (B5), we see that  $\vec{u}(s/\epsilon, \theta)$  has components that scale as

$$u_x\left(\frac{s}{\epsilon}\right) = 1 - \frac{Z\epsilon^3}{s^3}, \quad u_\theta\left(\frac{s}{\epsilon}\right) = 1 + \frac{2Z\epsilon^3}{s^3}, \quad (\text{B9})$$

where we neglect the  $e^{-s/\epsilon}$  dependence because it falls off faster than any power of  $\epsilon$  for  $\epsilon \ll 1$ . Because we only take the inner expansion to first order in  $\epsilon$ , we neglect the third-order terms in Eq. (B9). Therefore, Eq. (B8) becomes

$$0 = \nabla_s^2 X - \cos \theta \frac{\partial X}{\partial s} + \frac{\sin \theta}{s} \frac{\partial X}{\partial \theta}. \quad (\text{B10})$$

Because there is no explicit  $\epsilon$  dependence in Eq. (B10), we do not define a perturbative expansion for  $X$  as we do for  $\chi$ . Instead, we solve Eq. (B10) directly. We will see that the solution is an expansion whose coefficients can depend on  $\epsilon$ , and this dependence will be determined by the asymptotic

matching. The outer expansion satisfies the boundary condition at infinity,

$$X(s \rightarrow \infty, \theta) = c_0 a^3, \quad (\text{B11})$$

which accounts for the uniform background concentration  $c_0$ .

We perform the asymptotic matching by requiring  $\chi$  and  $X$  to have the same functional form in some common region where both expansions meet. This is achieved by matching the behavior of  $\chi$  as  $x \rightarrow \infty$  to that of  $X$  as  $s \rightarrow 0$ .

### 1. Outer expansion

We write the outer expansion in the form

$$X(s, \theta) = c_0 a^3 + \tilde{X}(s, \theta). \quad (\text{B12})$$

The first term satisfies the boundary condition in Eq. (B11) explicitly, and therefore  $\tilde{X}$  must vanish as  $s \rightarrow \infty$ . The first term also vanishes in Eq. (B10), and therefore  $\tilde{X}$  must solve Eq. (B10). The solution that vanishes at infinity is [2]

$$\tilde{X}(s, \theta) = \frac{e^{\frac{1}{2} \cos \theta}}{\sqrt{s}} \sum_{\ell=0}^{\infty} C_{\ell} K_{\ell+1/2}(s/2) Y_{\ell}^0(\theta), \quad (\text{B13})$$

where the  $Y_{\ell}^m$  are spherical harmonics, and the  $K$  are modified Bessel functions of the second kind. The coefficients  $C_{\ell}$  will be determined by the matching condition.

### 2. Inner expansion

Inserting Eq. (B6) into Eqs. (B3) and (B7), we see that, to zeroth order in  $\epsilon$ , we have

$$0 = \nabla_x^2 \chi_0 \quad (\text{B14})$$

with the boundary condition

$$-\partial_x \chi_0|_{x=1} = \beta - \alpha \chi_0(1, \theta). \quad (\text{B15})$$

The solution to Eq. (B14) possessing azimuthal symmetry is

$$\chi_0(x, \theta) = \sum_{\ell=0}^{\infty} \left( A_{0\ell} x^{\ell} + \frac{B_{0\ell}}{x^{\ell+1}} \right) Y_{\ell}^0(\theta). \quad (\text{B16})$$

Inserting Eq. (B16) into Eq. (B15) and noting that the spherical harmonics are linearly independent, we obtain the system

$$-\ell A_{0\ell} + (\ell + 1) B_{0\ell} = \sqrt{4\pi} \beta \delta_{0\ell} - \alpha (A_{0\ell} + B_{0\ell}), \quad (\text{B17})$$

where we have used the fact that  $Y_0^0 = 1/\sqrt{4\pi}$ . Because the Bessel functions in the outer expansion [Eq. (B13)] decrease as a function of  $s = \epsilon x$ , matching will fail if  $\chi_0$  contains terms that increase as a function of  $x$ . Therefore, we must have  $A_{0\ell} = 0$  for  $\ell > 0$ . Equation (B17) for  $\ell > 0$  then reads  $(\ell + 1) B_{0\ell} = -\alpha B_{0\ell}$ , but because  $\alpha$  is non-negative we must also have  $B_{0\ell} = 0$  for  $\ell > 0$ . Finally, Eq. (B17) for  $\ell = 0$  reads  $B_{00} = \sqrt{4\pi} \beta - \alpha (A_{00} + B_{00})$ , or  $B_{00} = (\sqrt{4\pi} \beta - \alpha A_{00}) / (1 + \alpha)$ . Together, these identifications reduce Eq. (B16) to

$$\chi_0(x) = \frac{A_{00}}{\sqrt{4\pi}} + \frac{\gamma}{x}, \quad (\text{B18})$$

where

$$\gamma \equiv \frac{\beta - \alpha A_{00} / \sqrt{4\pi}}{1 + \alpha}. \quad (\text{B19})$$

$A_{00}$  will be determined by the matching condition.

To first order in  $\epsilon$ , we have

$$0 = \nabla_x^2 \chi_1 - \vec{u} \cdot \vec{\nabla}_x \chi_0 \quad (\text{B20})$$

with the boundary condition

$$-\partial_x \chi_1|_{x=1} = -\alpha \chi_1(1, \theta). \quad (\text{B21})$$

Note that unlike in the outer expansion, which is valid far from the cell, in Eq. (B20) we must use the full form of  $\vec{u}$  [Eqs. (B4) and (B5)] because we are near the cell surface. The solution to Eq. (B20) possessing azimuthal symmetry is [2]

$$\begin{aligned} \chi_1(x, \theta) = & \frac{\gamma}{8} \sqrt{\frac{4\pi}{3}} F(x) Y_1^0(\theta) \\ & + \gamma \sum_{\ell=0}^{\infty} \left( A_{1\ell} x^{\ell} + \frac{B_{1\ell}}{x^{\ell+1}} \right) Y_{\ell}^0(\theta), \end{aligned} \quad (\text{B22})$$

where

$$\begin{aligned} F(x) = & 4 - \frac{4(2\zeta + 1)}{x^2} + \frac{2(1 + 3\zeta + 3\zeta^2)}{x^3} \\ & + \frac{\zeta^2 e^{1/\zeta}}{x^3} \left[ \left( \frac{x^3}{\zeta^3} - \frac{x^2}{\zeta^2} + \frac{2x}{\zeta} - 6 \right) e^{-x/\zeta} \right. \\ & \left. - \frac{x^4 E_1(x/\zeta)}{\zeta^4} \right], \end{aligned} \quad (\text{B23})$$

and  $E_1(y) \equiv \int_1^{\infty} dt e^{-ty}/t$ . Noting that  $F'(1) = F(1) = w$ , where

$$w \equiv 1 + \frac{1}{\zeta} - \frac{e^{1/\zeta} E_1(1/\zeta)}{\zeta^2}, \quad (\text{B24})$$

we insert Eq. (B22) into Eq. (B21) to obtain the system

$$\begin{aligned} & \sqrt{\frac{4\pi}{3}} \frac{w}{8} \delta_{1\ell} + \ell A_{1\ell} - (\ell + 1) B_{1\ell} \\ & = \alpha \left( \sqrt{\frac{4\pi}{3}} \frac{w}{8} \delta_{1\ell} + A_{1\ell} + B_{1\ell} \right). \end{aligned} \quad (\text{B25})$$

As before, because the Bessel functions in the outer expansion [Eq. (B13)] decrease as a function of  $s = \epsilon x$ , we must have  $A_{1\ell} = 0$  for  $\ell > 0$ . For  $\ell > 1$ , Eq. (B25) then reads  $(\ell + 1) B_{1\ell} = -\alpha B_{1\ell}$ , and again because  $\alpha$  is non-negative we must also have  $B_{1\ell} = 0$  for  $\ell > 1$ . Finally, for  $\ell = 1$  and 0, Eq. (B25) immediately implies  $B_{11} = \sqrt{4\pi}/3 (w/8) (1 - \alpha) / (2 + \alpha)$  and  $B_{10} = -\alpha A_{10} / (1 + \alpha)$ , respectively. Together, these identifications reduce Eq. (B22) to

$$\begin{aligned} \chi_1(x, \theta) = & \frac{\gamma A_{10}}{\sqrt{4\pi}} \left[ 1 - \frac{\alpha}{(1 + \alpha)x} \right] \\ & + \frac{\gamma}{8} \left[ F(x) + \frac{(1 - \alpha)w}{(2 + \alpha)x^2} \right] \cos \theta, \end{aligned} \quad (\text{B26})$$

where we have recognized that  $Y_1^0(\theta) = \sqrt{3/4\pi} \cos \theta$ .  $A_{10}$  will be determined by the matching condition.

### 3. Matching

The first two terms in the sum of the outer expansion [Eqs. (B12) and (B13)], which will be sufficient for the

matching condition, are

$$X(s, \theta) = c_0 a^3 + \frac{e^{-\frac{s}{2}(1-\cos\theta)}}{2s} \times \left[ C_0 + \sqrt{3}C_1 \left( 1 + \frac{2}{s} \right) \cos\theta + \dots \right], \quad (\text{B27})$$

where we have used  $K_{1/2}(s/2) = e^{-s/2} \sqrt{\pi/s}$  and  $K_{3/2}(s/2) = e^{-s/2} (1 + 2/s) \sqrt{\pi/s}$ . In the matching limit ( $s \rightarrow 0$ ) we expand the exponential,

$$X(s, \theta) = c_0 a^3 + \frac{1}{2s} \left[ 1 - \frac{s}{2}(1 - \cos\theta) + \dots \right] \times \left[ C_0 + \sqrt{3}C_1 \left( 1 + \frac{2}{s} \right) \cos\theta + \dots \right]. \quad (\text{B28})$$

For the inner expansion, it will be sufficient in the matching limit ( $x \rightarrow \infty$ ) to keep terms out to order  $1/x$ . To this order,  $F(x) = 4$  [Eq. (B23)], where we have neglected the  $e^{-x/\zeta}$  and  $E_1(x/\zeta)$  terms because they decay exponentially. Thus, the inner expansion [Eqs. (B6), (B18), and (B26)] becomes

$$\chi(x, \theta) = \frac{A_{00}}{\sqrt{4\pi}} + \frac{\gamma}{x} + \epsilon\gamma \left\{ \frac{A_{10}}{\sqrt{4\pi}} \left[ 1 - \frac{\alpha}{(1+\alpha)x} \right] + \frac{\cos\theta}{2} + \dots \right\}. \quad (\text{B29})$$

To match Eqs. (B28) and (B29), we equate like terms in  $x$  and  $\theta$ . The constant terms are

$$c_0 a^3 - \frac{C_0}{4} = \frac{A_{00}}{\sqrt{4\pi}} + \frac{\epsilon\gamma A_{10}}{\sqrt{4\pi}}. \quad (\text{B30})$$

The terms proportional to  $\cos\theta$  are

$$\frac{C_0}{4} - \frac{\sqrt{3}C_1}{4} = \frac{\epsilon\gamma}{2}. \quad (\text{B31})$$

Recalling that  $s = \epsilon x$ , the terms proportional to  $1/x$  are

$$\frac{C_0}{2\epsilon} = \gamma - \frac{\epsilon\gamma A_{10}\alpha}{\sqrt{4\pi}(1+\alpha)}. \quad (\text{B32})$$

Combining Eqs. (B31) and (B32) yields  $C_1 = [\gamma\alpha A_{10}/\sqrt{3\pi}(1+\alpha)]\epsilon^2$ . Assuming that  $A_{10}$  is order unity (which will be justified post hoc), we see that  $C_1$  is second order in  $\epsilon$  and must therefore be neglected because we only took  $\chi$  to first order in  $\epsilon$ . Neglecting  $C_1$ , Eq. (B31) implies

$$C_0 = 2\epsilon\gamma. \quad (\text{B33})$$

Then, equating terms in Eq. (B30) at each order in  $\epsilon$  yields

$$A_{00} = \sqrt{4\pi}c_0 a^3, \quad A_{10} = -\sqrt{\pi}. \quad (\text{B34})$$

This completes the matching up to first order in  $\epsilon$ , which is sufficient to obtain the anisotropy to this order at the cell surface from  $\chi$ .

#### 4. Anisotropy

In terms of  $\chi = ca^3$  and  $x = r/a$ , the expression for the anisotropy at the cell surface [Eq. (1)] reads

$$A = \frac{\int d\Omega \chi(1, \theta) \cos\theta}{\int d\Omega' \chi(1, \theta')}. \quad (\text{B35})$$

In the numerator, any term in  $\chi(1, \theta)$  that is constant in  $\theta$  will vanish upon integration. Therefore, the numerator will pick out only the term in  $\chi_1$  [Eq. (B26)] proportional to  $\cos\theta$ . In the denominator, the contribution from  $\chi_0$  [Eq. (B18)] is nonvanishing. Thus, to leading order in  $\epsilon$ ,

$$A = \frac{\int d\Omega \epsilon \chi_1(1, \theta) \cos\theta}{\int d\Omega' \chi_0(1)}. \quad (\text{B36})$$

Inserting the expressions for  $\chi_0$  and  $\chi_1$  yields

$$A = \frac{(\epsilon\gamma/8)[F(1) + w(1-\alpha)/(2+\alpha)] \int d\Omega \cos^2\theta}{(A_{00}/\sqrt{4\pi} + \gamma) \int d\Omega'}. \quad (\text{B37})$$

The integrals evaluate to  $\int d\Omega \cos^2\theta = \int_0^{2\pi} d\phi \int_0^\pi d\theta \sin\theta \cos^2\theta = 4\pi/3$  and  $\int d\Omega' = 4\pi$ . Recalling that  $F(1) = w$ , and inserting the expressions for  $A_{00}$  [Eq. (B34)] and  $\gamma$  [Eq. (B19)] and simplifying, we obtain

$$A = \frac{\epsilon w}{8(2+\alpha)} \frac{\beta - \alpha c_0 a^3}{\beta + c_0 a^3}. \quad (\text{B38})$$

In the limit of low permeability ( $\zeta = \sqrt{\kappa}/a \ll 1$ ), Eq. (B24) reduces to  $w = 2$ . With this value, and the original definitions  $\beta = va^2/4\pi D$  and  $\alpha = \mu/4\pi aD$ , Eq. (B38) becomes Eq. (4).

- [1] J. D. Shields, M. E. Fleury, C. Yong, A. A. Tomei, G. J. Randolph, and M. A. Swartz, Autologous chemotaxis as a mechanism of tumor cell homing to lymphatics via interstitial flow and autocrine CCR7 signaling, *Cancer Cell* **11**, 526 (2007).
- [2] S. Fancher, M. Vennettilli, N. Hilgert, and A. Mugler, Precision of Flow Sensing by Self-Communicating Cells, *Phys. Rev. Lett.* **124**, 168101 (2020).
- [3] W. J. Polacheck, J. L. Charest, and R. D. Kamm, Interstitial flow influences direction of tumor cell migration through competing mechanisms, *Proc. Natl. Acad. Sci. (USA)* **108**, 11115 (2011).

- [4] J. M. Munson, R. V. Bellamkonda, and M. A. Swartz, Interstitial flow in a 3d microenvironment increases glioma invasion by a CXCR4-dependent mechanism, *Cancer Res.* **73**, 1536 (2013).
- [5] C.-L. E. Helm, M. E. Fleury, A. H. Zisch, F. Boschetti, and M. A. Swartz, Synergy between interstitial flow and VEGF directs capillary morphogenesis in vitro through a gradient amplification mechanism, *Proc. Natl. Acad. Sci. (USA)* **102**, 15779 (2005).
- [6] A. S. Khair, Two-cell interactions in autologous chemotaxis, *Phys. Rev. E* **104**, 024404 (2021).

- [7] D. Kobayashi, M. Endo, H. Ochi, H. Hojo, M. Miyasaka, and H. Hayasaka, Regulation of CCR7-dependent cell migration through CCR7 homodimer formation, *Sci. Rep.* **7**, 8536 (2017).
- [8] M. A. Byers, P. A. Calloway, L. Shannon, H. D. Cunningham, S. Smith, F. Li, B. C. Fassold, and C. M. Vines, Arrestin 3 mediates endocytosis of CCR7 following ligation of CCL19 but not CCL21, *J. Immunol.* **181**, 4723 (2008).
- [9] R. G. Endres and N. S. Wingreen, Accuracy of direct gradient sensing by single cells, *Proc. Natl. Acad. Sci. (USA)* **105**, 15749 (2008).
- [10] J. Varennes, S. Fancher, B. Han, and A. Mugler, Emergent Versus Individual-Based Multicellular Chemotaxis, *Phys. Rev. Lett.* **119**, 188101 (2017).
- [11] H. C. Brinkman, A calculation of the viscous force exerted by a flowing fluid on a dense swarm of particles, *Flow, Turb. Combust.* **1**, 27 (1949).
- [12] <https://github.com/gonzalezlouis/AutologousChemotaxis>.
- [13] M. E. Fleury, K. C. Boardman, and M. A. Swartz, Autologous morphogen gradients by subtle interstitial flow and matrix interactions, *Biophys. J.* **91**, 113 (2006).
- [14] H. C. Berg and E. M. Purcell, Physics of chemoreception, *Biophys. J.* **20**, 193 (1977).
- [15] A. Mugler, A. Levchenko, and I. Nemenman, Limits to the precision of gradient sensing with spatial communication and temporal integration, *Proc. Natl. Acad. Sci. (USA)* **113**, E689 (2016).
- [16] J. Korbecki, S. Grochans, I. Gutowska, K. Barczak, and I. Baranowska-Bosiacka, Cc chemokines in a tumor: A review of pro-cancer and anti-cancer properties of receptors CCR5, CCR6, CCR7, CCR8, CCR9, and CCR10 ligands, *Int. J. Molec. Sci.* **21**, 7619 (2020).
- [17] Y. Lin, S. Sharma, and M. St John, Ccl21 cancer immunotherapy, *Cancers* **6**, 1098 (2014).
- [18] S. Sharma, P. Kadam, and S. Dubinett, Ccl21 programs immune activity in tumor microenvironment, *Tumor Microenviron.* **1231**, 67 (2020).
- [19] H.-W. Cheng, L. Onder, J. Cupovic, M. Boesch, M. Novkovic, N. Pikor, I. Tarantino, R. Rodriguez, T. Schneider, W. Jochum *et al.*, Ccl19-producing fibroblastic stromal cells restrain lung carcinoma growth by promoting local antitumor T-cell responses, *J. Allergy Clin. Immunol.* **142**, 1257 (2018).
- [20] R. Bouffanais, J. Sun, and D. K. P. Yue, Physical limits on cellular directional mechanosensing, *Phys. Rev. E* **87**, 052716 (2013).
- [21] R. M. Enmon Jr., K. C. O'Connor, D. J. Lacks, D. K. Schwartz, and R. S. Dotson, Dynamics of spheroid self-assembly in liquid-overlay culture of DU 145 human prostate cancer cells, *Biotechnol. Bioeng.* **72**, 579 (2001).
- [22] R. M. Enmon Jr., K. C. O'Connor, H. Song, D. J. Lacks, and D. K. Schwartz, Aggregation kinetics of well and poorly differentiated human prostate cancer cells, *Biotechnol. Bioeng.* **80**, 580 (2002).
- [23] P. Friedl and D. Gilmour, Collective cell migration in morphogenesis, regeneration and cancer, *Natl. Rev. Mol. Cell Biol.* **10**, 445 (2009).
- [24] K. J. Cheung, E. Gabrielson, Z. Werb, and A. J. Ewald, Collective invasion in breast cancer requires a conserved basal epithelial program, *Cell* **155**, 1639 (2013).
- [25] A. Puliafito, A. De Simone, G. Seano, P. A. Gagliardi, L. Di Blasio, F. Chianale, A. Gamba, L. Primo, and A. Celani, Three-dimensional chemotaxis-driven aggregation of tumor cells, *Sci. Rep.* **5**, 15205 (2015).
- [26] O. Zajac, J. Raingeaud, F. Libanje, C. Lefebvre, D. Sabino, I. Martins, P. Roy, C. Benatar, C. Canet-Jourdan, P. Azorin *et al.*, Tumour spheres with inverted polarity drive the formation of peritoneal metastases in patients with hypermethylated colorectal carcinomas, *Nat. Cell Biol.* **20**, 296 (2018).
- [27] M. Sarris, R. Olekhnovitch, and P. Bouso, Manipulating leukocyte interactions in vivo through optogenetic chemokine release, *Blood, J. Am. Soc. Hematol.* **127**, e35 (2016).
- [28] T. Gregor, D. W. Tank, E. F. Wieschaus, and W. Bialek, Probing the limits to positional information, *Cell* **130**, 153 (2007).
- [29] S. C. Little, M. Tikhonov, and T. Gregor, Precise developmental gene expression arises from globally stochastic transcriptional activity, *Cell* **154**, 789 (2013).
- [30] T. Erdmann, M. Howard, and P. R. Ten Wolde, Role of Spatial Averaging in the Precision of Gene Expression Patterns, *Phys. Rev. Lett.* **103**, 258101 (2009).
- [31] W. J. Rosoff, J. S. Urbach, M. A. Esrick, R. G. McAllister, L. J. Richards, and G. J. Goodhill, A new chemotaxis assay shows the extreme sensitivity of axons to molecular gradients, *Nat. Neurosci.* **7**, 678 (2004).
- [32] G. Malet-Engra, W. Yu, A. Oldani, J. Rey-Barroso, N. S. Gov, G. Scita, and L. Dupré, Collective cell motility promotes chemotactic prowess and resistance to chemorepulsion, *Curr. Biol.* **25**, 242 (2015).
- [33] D. Ellison, A. Mugler, M. D. Brennan, S. H. Lee, R. J. Huebner, E. R. Shamir, L. A. Woo, J. Kim, P. Amar, I. Nemenman, A. J. Ewald, and A. Levchenko, Cell-cell communication enhances the capacity of cell ensembles to sense shallow gradients during morphogenesis, *Proc. Natl. Acad. Sci. (USA)* **113**, E679 (2016).
- [34] B. A. Camley, J. Zimmermann, H. Levine, and W.-J. Rappel, Emergent Collective Chemotaxis Without Single-Cell Gradient Sensing, *Phys. Rev. Lett.* **116**, 098101 (2016).
- [35] S. Fancher and A. Mugler, Fundamental Limits to Collective Concentration Sensing in Cell Populations, *Phys. Rev. Lett.* **118**, 078101 (2017).
- [36] B. Barman, Flow of a Newtonian fluid past an impervious sphere embedded in a porous medium, *Ind. J. Pure Appl. Math.* **27**, 1249 (1996).
- [37] A. Acrivos and T. D. Taylor, Heat and mass transfer from single spheres in Stokes flow, *Phys. Fluids* **5**, 387 (1962).